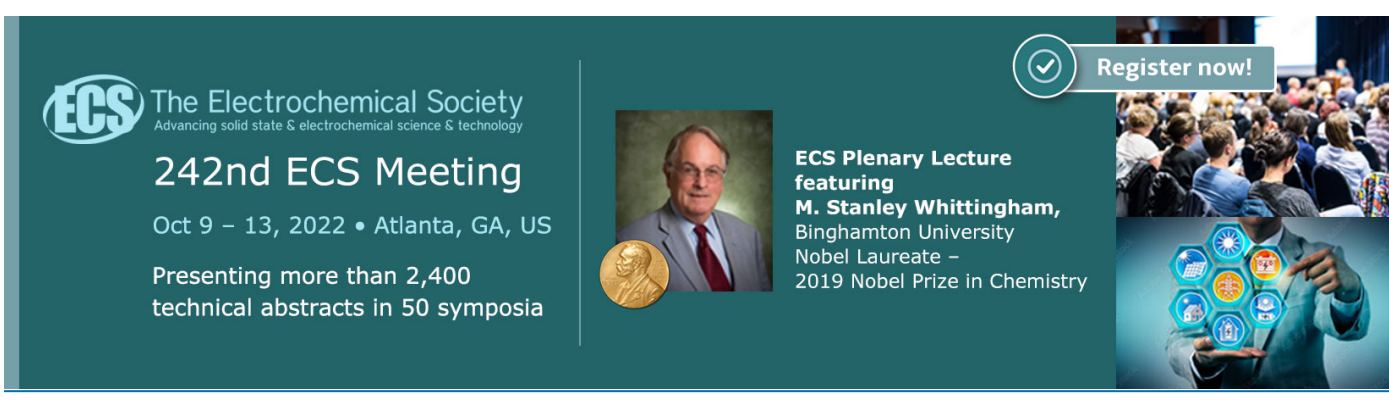


Successive Phase Transitions and Multiferroicity in Deformed Triangular-Lattice Antiferromagnets $Ca_3MNb_2O_9$ (M=Co, Ni) with Spatial Anisotropy

To cite this article: Q. Huang et al 2022 ECS J. Solid State Sci. Technol. 11 063004

View the article online for updates and enhancements.







Successive Phase Transitions and Multiferroicity in Deformed Triangular-Lattice Antiferromagnets Ca₃MNb₂O₉ (M=Co, Ni) with Spatial Anisotropy

Q. Huang, M. Lee, ² E. S. Choi, J. Ma, C. Dela Cruz, and H. D. Zhou La Cruz,

We constructed the magnetic field-temperature phase diagrams of new quasi-two-dimensional isosceles triangular lattice antiferromagnets (TLAF) $Ca_3MNb_2O_9$ (M=Co, Ni) from dc and ac magnetic susceptibilities, specific heat, dielectric constant, and electric polarization measurements on *single crystalline* samples. $Ca_3CONb_2O_9$ with effective spin-1/2 Co^{2+} ions undergoes a two-step antiferromagnetic phase transition at $T_{N1}=1.3$ K and $T_{N2}=1.5$ K and enters a stripe ordered state at zero magnetic field. With increasing field, successive magnetic phase transitions, reminiscent of the up-up-down (*uud*) and the oblique phases, are observed. The dielectric constant of $Ca_3CONb_2O_9$ shows anomalies related to the magnetic phase transitions, but clear evidence of ferroelectricity is absent. Meanwhile, $Ca_3NiNb_2O_9$ with spin-1 Ni^{2+} ions also shows a two-step antiferromagnetic transition at $T_{N1}=3.8$ K and $T_{N2}=4.2$ K at zero field. For $Ca_3NiNb_2O_9$, the electric polarization in the magnetic ordered phases was clearly observed from the pyroelectric current measurements, which indicates its coexistence of magnetic ordering and ferroelectricity.

© 2022 The Electrochemical Society ("ECS"). Published on behalf of ECS by IOP Publishing Limited. [DOI: 10.1149/2162-8777/ac7254]

Manuscript submitted December 11, 2021; revised manuscript received May 6, 2022. Published June 3, 2022. This paper is part of the JSS Focus Issue on Focus Issue In Honor of John Goodenough: A Centenarian Milestone.

The geometrically frustrated magnetism (GFM) is an energetic field of research in condensed matter magnetism. The frontier of the GFM research has been greatly expanded from the prediction of the exotic quantum spin liquid^{1,2} to the ubiquitous topological physics. As an archetype of geometrically frustrated systems, triangular lattice antiferromagnets (TLAFs) have provided a playground for extensive theoretical and experimental studies on the GFM, which have led to a better understanding of the underlying physics of the GFM. Historically, it was pointed out that the Ising spins residing in a triangular lattice fail to order, leaving massive residual entropy even at zero temperature, an apparent violation of the third law of thermodynamics.⁴ Anderson predicted so-called quantum spin liquid, an exotic ground state in the context of strongly fluctuating antiferromagnetically correlated S-1/2 Heisenberg spins, and further proposed it as a possible mechanism to realize high-T_c superconductivity in a triangular lattice system. 1,5 On the other hand, the theories suggested that TLAFs with nearest-neighbor (NN) interaction have a long-range ordering state at zero temperature with reduced sublattice magnetizations. ⁶⁻⁹ The spin structure of the longrange ordered state is called a coplanar 120 degree state, in which three spins in a triangular plaquette point at 120 degrees from one another in the same plane.

In the presence of an external magnetic field, the theories predicted that the ground state should satisfy the constraint of $\mathbf{M} = \mathbf{H}/(3\,\mathrm{J})$, where \mathbf{M} , \mathbf{H} , and \mathbf{J} are net magnetization of a triangular plaquette, magnetic field, and NN exchange interaction, respectively. However, a unique minimum energy state cannot be selected under this constraint. Consequently, massive degeneracies continue until the magnetization is fully saturated. Therefore, the ground state at a finite magnetic field of a TLAF is ultimately determined by either quantum fluctuations for small spins 12,13 or thermal fluctuations for large spins. 10,11,14 The most celebrated phase is the one-third magnetization plateau with up-up-down (UUD) spin structure around $\mathbf{H} \sim 3\,\mathrm{J}$. In general, two additional states are also stabilized at lower and higher fields of the UUD phase: (1) Y state at lower fields, a tilted version of the 120 degree

state, (2) oblique phase at higher fields, a canted version of UUD phase. And the oblique phase can be further classified into V, V' and φ phase based on the difference in symmetry. Experimentally, these phases have been observed in some triple-perovskite systems, $Ba_3MB_2O_9$ (M=Co, Ni and B=Sb, Nb, Ta), which are reported to be TLAFs. $^{15-22}$ In the compounds with B=Sb, Nb, the UUD phase exists and is stabilized in a wider range of magnetic field at lower temperatures due to quantum fluctuations. $^{15-19,21}$ However, the compounds with B=Ta don't show UUD phase. 20,21,23 The understanding of the successive magnetic phase transitions in TLAFs has helped to study the exotic magnetism in such systems.

Another important aspect of the TLAF research is related to its multiferroicity, which has been another vibrant field of research in the last decade. ^{24–28} It was proposed that frustration driven multiferroicity can overcome the weak magnetoelectric effect observed in the conventional type I multiferroic compounds. ²⁹ Several microscopic models ^{30–32} and phenomenological ³³ theories have been proposed to describe the strong coupling between the non-collinear antiferromagnetic phase and the ferroelectricity. It was also pointed out that both spin chirality and spin helicity are relevant order parameters for the multiferroicity. ³⁴ A recent study suggested that the multiferroicity in the Y phase of RbFe(MoO₄)₂ is mainly associated with the spin chirality. ³⁵ More enigmatic multiferroic phases have been found in Ba₃CoNb₂O₉(Co²⁺, S = 1/2), ¹⁷ and Ba₃NiNb₂O₉(Ni²⁺, S = 1). ¹⁸ In these compounds, ferroelectricity emerges unexpectedly in all magnetically ordering phases, including the collinear phases. While Ba₃CoSb₂O₉ with similar magnetically ordered phases doesn't show any ferroelectricity. Therefore, the picture of multiferroicity in TLAF is still incomplete.

In all the Ba₃MB₂O₉ systems described above, the magnetic ions (M ions) form an equilateral triangular lattice. Meanwhile, it has been reported that the substitution of Ba with Ca can lead to a lattice distortion in Ca₃MB₂O₉, and therefore forms an isosceles triangular lattice of the M ions.²² In this work, we aim to study the effects on magnetism due to this spatial anisotropy induced by the lattice distortion in the TLAFs. Single crystalline isosceles TLAFs, Ca₃CoNb₂O₉ (Co²⁺, S = 1/2) and Ca₃NiNb₂O₉ (Ni²⁺, S = 1) were prepared for this purpose. Our previous study reported that in Ca₃NiNb₂O₉, such lattice distortion doesn't change the 120 degree

¹Department of Physics and Astronomy, University of Tennessee, Knoxville, Tennessee 37996-1200, United States of America

²National High Magnetic Field Laboratory, Florida State University, Tallahassee, Florida 32310-3706, United States of America

³Key Laboratory of Artificial Structures and Quantum Control (Ministry of Education), Shenyang National Laboratory for Materials Science, School of Physics and Astronomy, Shanghai Jiao Tong University, Shanghai, People's Republic of China ⁴Quantum Condensed Matter Division, Oak Ridge National Laboratory, Oak Ridge, Tennessee 37831, United States of America

ordering state. ²⁴ However, in this study, we found that the magnetic ordered state under zero field in Ca₃CoNb₂O₉ is not a 120 degree ordering state anymore, but a stripe ordered state through neutron diffraction measurements. The DC and AC susceptibility, specific heat measurements were also performed to construct the magnetic phase diagrams of Ca₃CoNb₂O₉ and Ca₃NiNb₂O₉. Furthermore, the dielectric constant and pyroelectric current measurements suggest the absence of ferroelectricity in Ca₃CoNb₂O₉ but the coexistence of ferroelectricity and magnetic ordered phases in Ca₃NiNb₂O₉, hence it is multiferroic. This difference could be related to their different magnetic ground states.

Experimental

Single crystalline $Ca_3MNb_2O_9$ (M=Co, Ni) was prepared using the traveling-solvent floating-zone method. The feed and seed rods for the crystal growth were made by a solid-state reaction. Stoichiometric mixtures of $CaCO_3$, CoO/NiO, and Nb_2O_5 were ground together and pressed into a 6 mm-diameter 60 mm-long rod under 400 atm hydrostatic pressure and annealed in air at 1350 °C (1230 °C) for 40 h. Then the single crystal growth was carried out in the air in an IR-heated image furnace equipped with two halogen lamps and double ellipsoidal mirrors with feed and seed rod rotating in opposite directions at 25 rpm. The crystal grew at a rate of 10 mm h $^{-1}$. The single-crystal samples were oriented using the Laue back diffraction technique. The rods of the pure polycrystalline sample were also used in neutron powder diffraction measurements.

High-resolution neutron powder diffraction (NPD) measurements were performed by a neutron powder diffractometer, HB2A, at the High flux of Oak Ridge National Laboratory. Around 3 g of powder sample were loaded in an Al-cylinder can and mounted in a closed-cycle refrigerator. The neutron wavelength is $\lambda=1.5424$ Å with a collimation of 120-open-60. The diffraction data were analyzed by the Rietveld refinement with the program FullProf. Neutron diffraction measurements were performed by the triple-axis spectrometer (HB-1A) at HFIR, ORNL. At HB-1A, the diffraction data were collected at 0.3 K and 5 K with the wavelength $\lambda=2.36$ Å. From the magnetic wavevector of (n₁ +/- 1/3, n₂ +/- 1/3, n₃ +/- 1/3), 20 magnetic Bragg peaks had been measured.

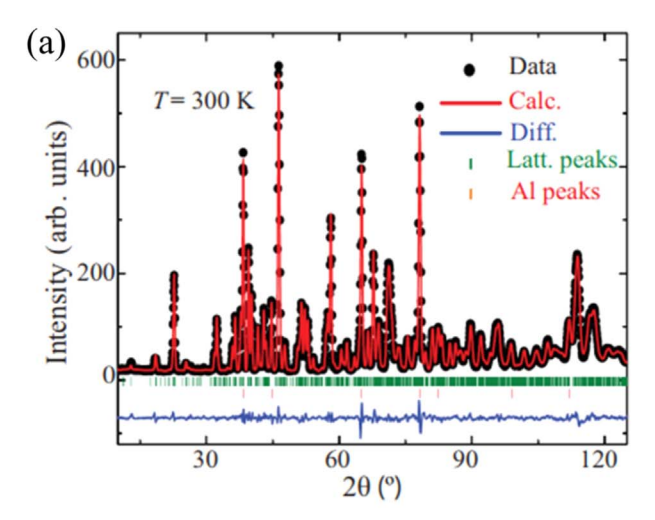
The DC magnetic susceptibility measurements were performed using a commercial SQUID magnetometer (MSPS, Quantum Design) and a vibrating sample magnetometer at the Nation High Magnetic Field Laboratory. AC susceptibility was measured with the conventional mutual inductance technique with the ac coils and sample immersed in He-3 liquid or a mixing chamber of a dilution fridge.

The specific heat data were obtained using a commercial physical property measurement system (PPMS, Quantum Design).

For the dielectric constant and polarization measurements, samples were polished to have a parallel capacitor geometry with typical dimensions of 4.7 mm² * 0.4 mm. Silver epoxy was painted on the two opposite parallel surfaces for the electrical contacts. A commercial capacitance bridge (Andeen-Hagerling, AH-2700A model) was used to measure the dielectric constant. The external magnetic and electric fields were applied parallel to the a and c* axis of the monoclinic system. The polarization measurements were performed on the same set of samples prepared for the dielectric constant measurements. The pyroelectric current was recorded while the temperature was rapidly increased $\sim 10 \, \mathrm{K \ min^{-1}}$ under various magnetic fields. To calculate the polarization, the pyroelectric currents were integrated in the time domain. The electric fields along the a-axis and c*-axis were 700 kV m⁻¹ and 590 kV m⁻¹, respectively, while cooling down the samples to form monodomains that give rise to maximized the pyroelectric current signal.

Results

Lattice and magnetic structure.—The NPD pattern of the polycrystalline Ca₃CoNb₂O₉ at 300 K is presented in Fig. 1a. No additional impurity peak is found in the whole diffraction range from 10° to



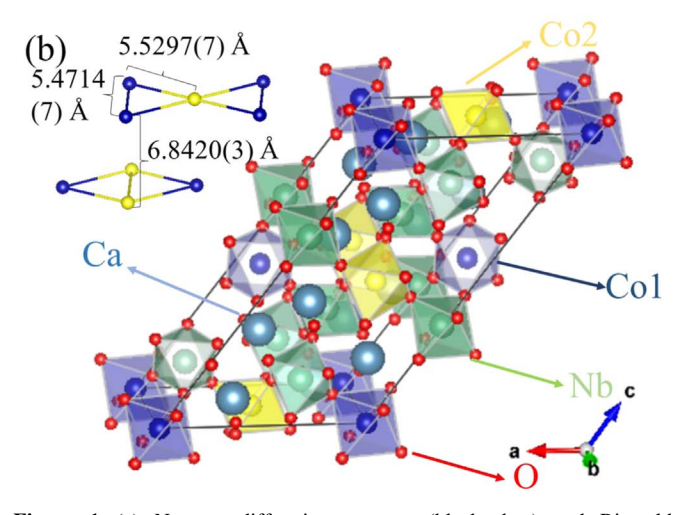


Figure 1. (a) Neutron diffraction patterns (black dots) and Rietveld refinements (red line) for $Ca_3CoNb_2O_9$ at 300 K. Blue line at the bottom of each panel is the difference curve. The green and red ticks are the reflection positions for the nuclear phases and Al-can, respectively. The refinements were done with the P121/c1 space group. (b) The lattice structure with the Co-triangular lattice of $Ca_3CoNb_2O_9$. The blue and yellow spheres represent Co1 and Co2 on two different sites, respectively.

125°. Similar to the previous reports, 37,38 the diffraction pattern could be fitted with a monoclinic unit cell with a =9.6104(4) Å, b =5.4717(7) Å, c =16.8532(3) Å, and $\beta=125.713(4)^\circ$. The space group is P121/c1 with cobalt atoms at 2a (0, 0, 0) site and 2d (1/2, 1/2, 0) site. The other atoms (Ca, Nb, and O) are all located at the 8 f (x, y, z) site. Detailed information of the atomic coordinates is shown in Table I. The final weighted residual error $R_{\rm wp}=3.12$. The lattice structure of Ca₃NiNb₂O₉ is isostructural to that of Ca₃CoNb₂O₉, which was confirmed by our previous NPD measurement reported in. 22 It also has a P121/c1 space group with a =9.5695(8) Å, b =5.4472(2) Å, c =16.7876(3) Å, and $\beta=125.718(3)^\circ$.

Unlike the hexagonal Ba-based triple-perovskites, Ba₃MB₂O₉ (M=Co, Ni, Mn, and B=Nb, Sb) with one M atomic position, the lattice distortion from hexagonal to monoclinic structure in Ca₃MNb₂O₉ leads to two M atomic positions. Although the M-triangular layers still exist in the ab plane, the *c* axis now is not perpendicular to those triangular planes. For example, in Ca₃CoNb₂O₉, the isosceles Co-triangle in ab plane now has one short side (Co1-Co1 5.4714(7) Å) and two long sides (Co1-Co2 5.5297(7) Å), respectively. The magnetic Co-layers are apart by 6.8420(3) Å and separated by the two non-magnetic Nb layers. For Ca₃NiNb₂O₉, the short side is 5.4472(2) Å and the long side is

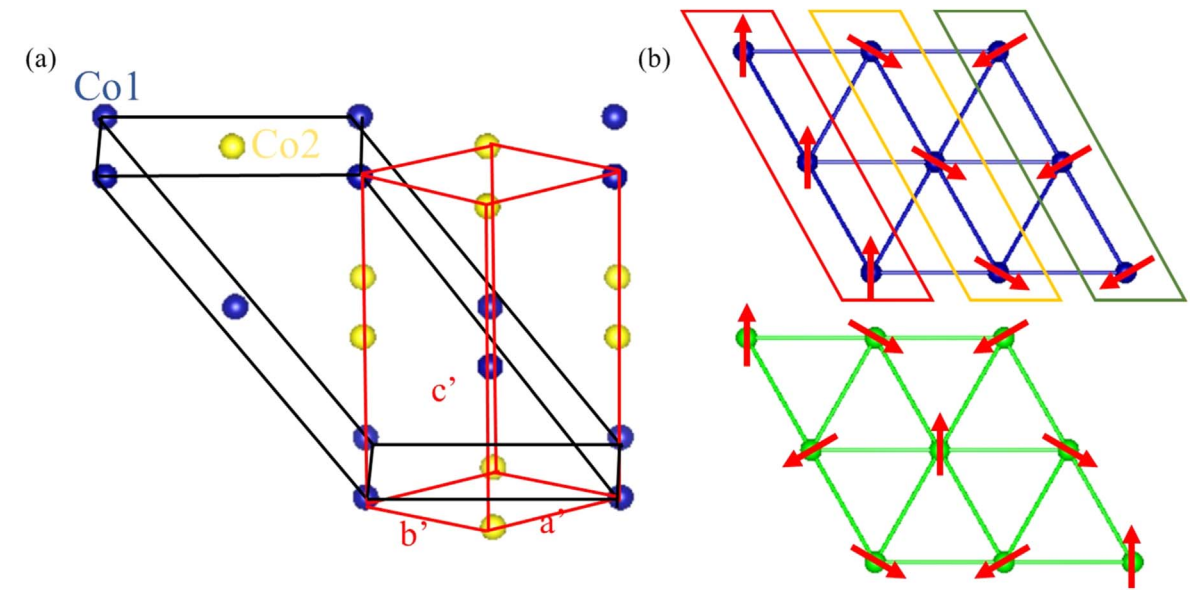


Figure 2. (a) Illustration of the transform of the unit cell from monoclinic (blue) to hexagonal (red) for Ca₃CoNb₂O₉. Here only the Co₁ (blue sphere) and Co₂ (yellow sphere) are plotted. (b)The stripe spin structure proposed for Ca₃CoNb₂O₉ (blue) and the 120 degree spin structure for Ca₃NiNb₂O₉ (green).

Table I. Structural parameters of Ca ₃ CoNb ₂ O ₉ at 300 K.					
Atom	site	X	y	z	Occ.
Ca1	4e	0.2496(2)	0.4962(3)	0.0661(9)	1
Ca2	4e	0.7549(2)	0.0057(3)	0.1004(9)	1
Ca3	4e	0.2548(2)	0.0317(16)	0.2339(11)	1
Co1	2a	0.0000	0.0000	0.0000	1
Co2	2d	0.5000	0.5000	0.0000	1
Nb1	4e	0.5019(14)	0.4872(19)	0.3345(8)	1
Nb2	4e	-0.0008(7)	-0.0049(20)	0.3394(7)	1
O1	4e	0.9516(17)	0.7134(21)	0.2473(11)	1
O2	4e	0.5466(14)	0.7875(21)	0.2851(8)	1
O3	4e	0.2547(22)	0.5921(18)	0.2626(10)	1
O4	4e	0.9736(14)	0.7108(20)	0.9254(8)	1
O5	4e	0.0481(17)	0.2068(20)	0.9168(10)	1
O6	4e	0.4509(14)	0.3262(17)	0.8867(9)	1
O7	4e	0.5575(17)	0.8083(19)	0.9469(9)	1
O8	4e	0.7445(22)	0.0982(19)	0.9101(9)	1
O9	4e	0.2426(18)	0.5840(19)	0.9270(8)	1

5.5056(5) Å, and with interlayer Ni–Ni distance 6.815 Å. It is noted that the interlayer distance of $Ca_3CoNb_2O_9$ is shorter than that of $Ba_3CoNb_2O_9$ (7.0808(3) Å)¹⁷ due to the monoclinic structure. Based on this structure, the applied field in the following measurements is parallel to the triangular lattice plane (a-axis) and perpendicular to the triangular plane (c*-axis), respectively.

The single-crystal neutron diffraction measurements on $Ca_3CoNb_2O_9$ performed at 300 mK indicate a propagation vector (1/3 1/3 1/3) in the monoclinic system. As shown in Fig. 2a, if we only take the magnetic ions Co^{2+} into consideration, we can still treat this system as a slightly distorted hexagonal lattice with a = b = 5.5208(9) Å, c = 13.668(3) Å, $\alpha = 89.182(13)^\circ$, $\beta = 90.818(13)^\circ$, and $\gamma = 120.704(12)^\circ$. Such a small distortion allows us to simplify the refinement of the magnetic structure by working on this hexagonal lattice with one Co ions site (0 0 0). The propagation vector can be thus transformed to be (1/3 0 2/3) in the hexagonal structure. Due to the limited number of magnetic peaks and the resolution of the data, we can't exactly solve the magnetic structure. However, the k vector (1/3 0 2/3) clearly leads to a stripe ordering model, as illustrated in Fig. 2b. The c component of each spin can't be solved by our data. If only

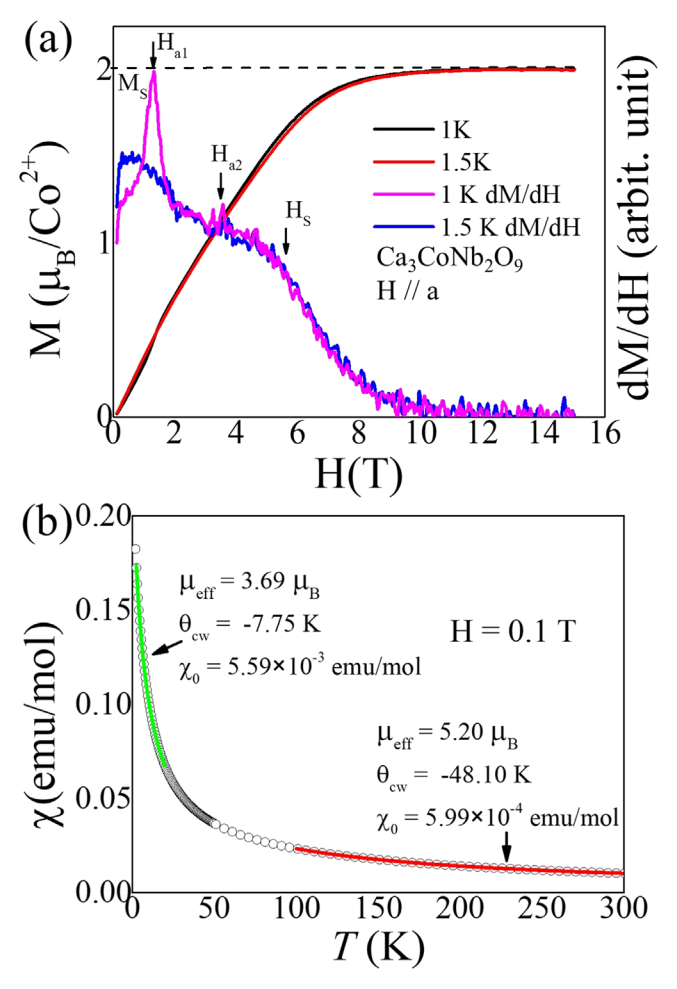


Figure 3. (a) The isothermal dc magnetization curve and its derivative (dM/dH) of $Ca_3CoNb_2O_9$ measured at 1.0 K and 1.5 K with H//a. (b) Temperature dependence of the dc susceptibility measured at 0.1 T. The solid lines show the fittings to data with Curie-Weiss formula including χ_0 term, $\chi = \chi_0 + C/(T - \theta_{cw})$, at two different temperature regions ($T \le 20$ K for the green line and 100 K $\le T \le 300$ K for the red line).

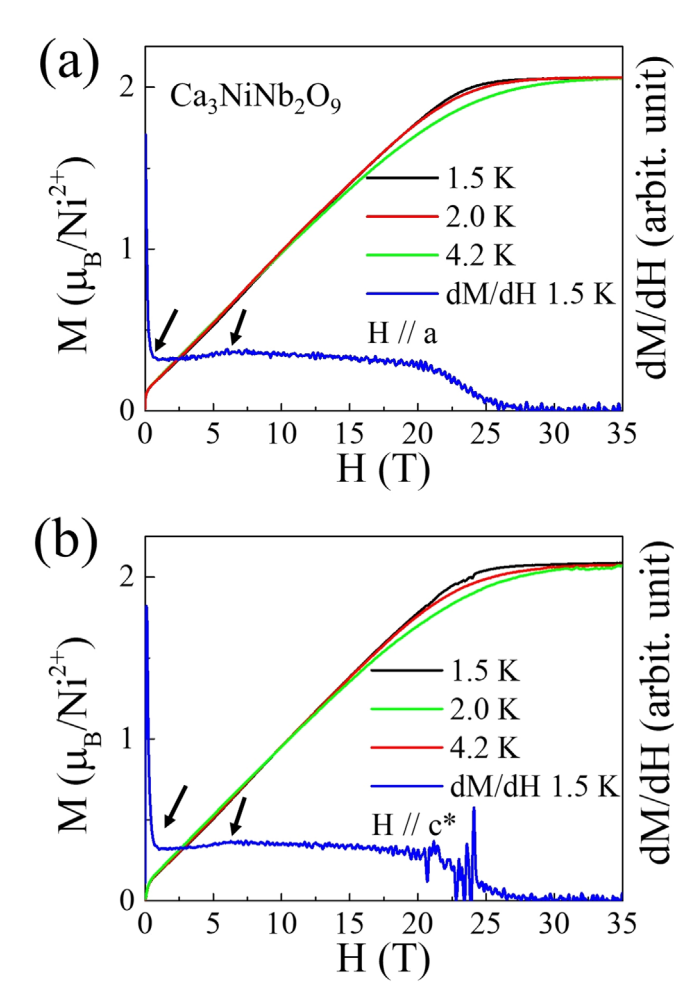


Figure 4. (a) The isothermal dc magnetization curve and its derivative (dM/dH) of $Ca_3NiNb_2O_9$ measured at 1.0 K, 2.0 K and 4.2 K up to 35 T with H//a (a) and H//c* axis (b). The arrows represent the field positions at which the anomalies were observed on the dM/dH curves.

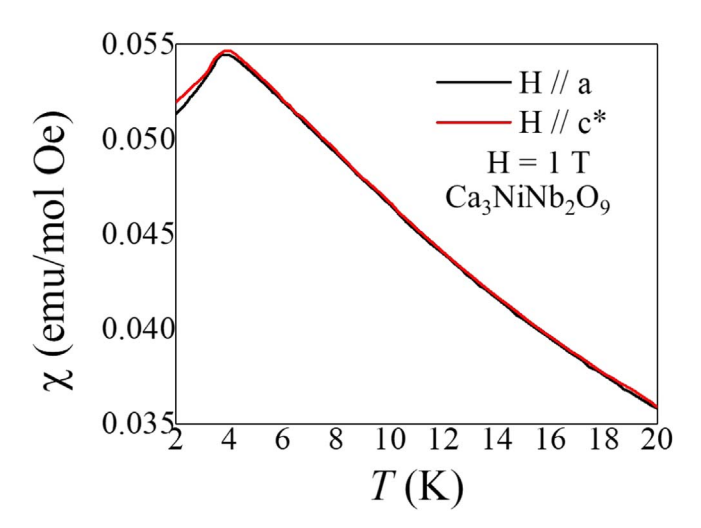


Figure 5. Temperature dependence of dc susceptibility of ${\rm Ca_3NiNb_2O_9}$ measured at 1 T.

considering the spin projections in the ab plane, we can tell that along one long side of the triangular, all the spin projections are parallel to each other. And along the other long side as well as the short side, the spin projections are 120° from the nearest neighbor spins. Such a "triple stripe" magnetic structure is quite different

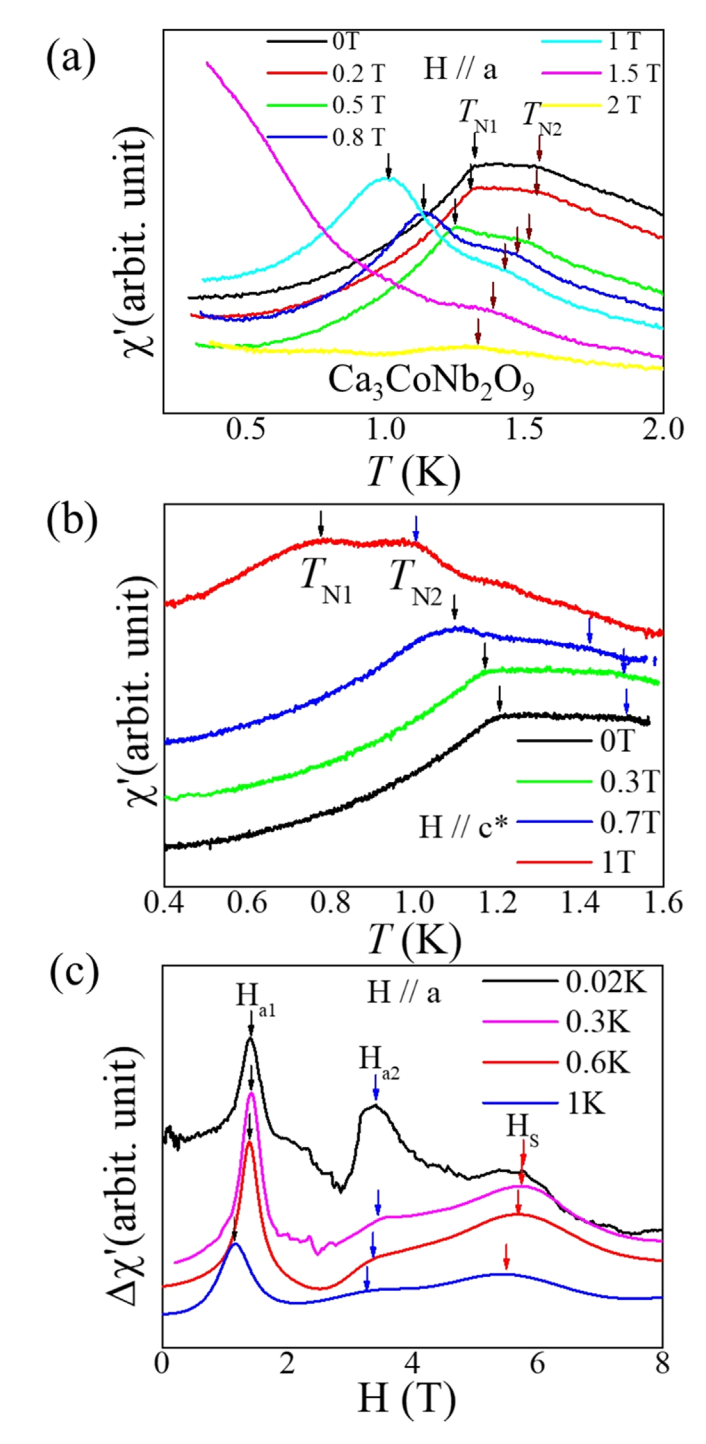


Figure 6. (a) The temperature dependence of ac susceptibility measured with dc field H//a. (b) The temperature dependence of ac susceptibility measured with dc field H//c*-axis. (c) The field dependence of ac susceptibility with the dc field H//a.

from the typical 120 degree spin structure predicted in TLAFs or observed in $Ca_3NiNb_2O_9$ shown in Fig. 2b.²²

DC and AC susceptibility.—The isothermal (T=1.0 and 1.5 K) DC magnetization curves of $Ca_3CoNb_2O_9$ with applied magnetic field H//a are shown in Fig. 3a. The first derivative of the magnetization (dM/dH) at T=1.0 K exhibits a very sharp peak around $H_{a1}=1.3$ T, followed by a small peak around $H_{a2}=3.4$ T. Although one-third magnetization (1/3 M_s) is close to H_{a1} , the expected magnetization plateau with 1/3 M_s in the UUD phase is not

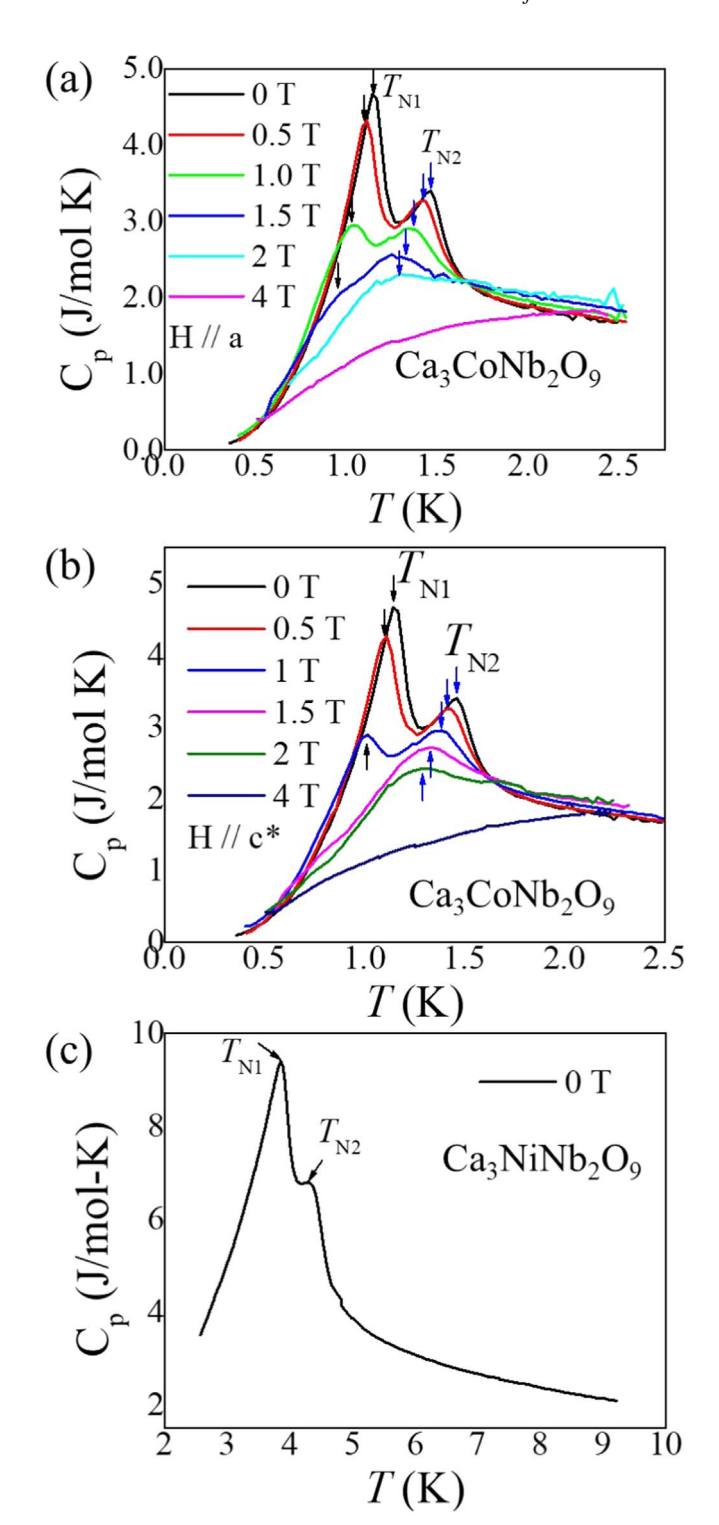


Figure 7. The temperature dependence of specific heat of $Ca_3CoNb_2O_9$ with H//a (a) and H//c* (b). (c) The temperature dependence of specific heat of $Ca_3NiNb_2O_9$ at zero field.

clearly observed. Nevertheless, the features of the dM/dH at the location of the 1/3 M_s still suggest that UUD phase is stabilized between H_{a1} and H_{a2} . The saturation field $H_s = 5.7$ T was assigned at the broad hump on the first derivative with a saturation moment 2.0 μ B/Co²⁺, which leads to a g-factor as 4. The g-factor is rather large, suggesting a strong spin-orbit coupling due to the orbital degeneracy. From this saturation field and the relation $g\mu_B\mu_0H_s = 9JS$ for a triangular lattice, ¹¹ we obtained a nearest neighbor exchange interaction $J \sim 3.4(3)$ K. Figure 3b shows the temperature

dependence of the DC magnetic susceptibility χ of the polycrystal-line Ca₃CoNb₂O₉ sample at 0.1 T down to 2 K. The fittings with the formula $\chi = \chi_0 + C/(T-\theta_{\rm CW})$ to $\chi(T)$ curve yield $\mu_{\rm eff} = 5.20~\mu_{\rm B}$, $\theta_{\rm CW} = -48.1~{\rm K}$, $\chi_0 = 5.99~\times~10^{-4}~{\rm emu~mol}^{-1}$ for the high temperature region and $\mu_{\rm eff} = 3.69~\mu_{\rm B}$, $\theta_{\rm CW} = -7.75~{\rm K}$, $\chi_0 = 5.59~\times~10^{-3}~{\rm emu~mol}^{-1}$ for low temperature region. The effective magnetic moment values agree well with a previous report. The negative Weiss temperature indicates an antiferromagnetic spin-exchange interaction. The decrease of effective moment indicates a crossover of spin state for Co²⁺ ions from high (S = 3/2) to low (S = 1/2) spin state due to the spin-orbital coupling, which is commonly observed in other Co-oxides with Co²⁺ ions in an octahedral environment. The decrease of the spin-orbital coupling is an octahedral environment.

Figure 4 shows isothermal (T=1.5, 2.0 and $4.2 \, \rm K$) DC magnetization and its first derivative ($T=1.5 \, \rm K$) of single crystal Ca₃NiNb₂O₉ with H//a (a) and H//c* (b). The two sets of magnetization curves show similar behavior. They exhibit a fast increase near the zero field and then a nearly linear increase before saturation. In the first derivative curves, a valley showed up near zero field, representing a spin-flip transition. And a small bump was observed around 7 T, suggesting a weak slope change. The saturation field assigned at the broad hump is around 20 T with saturation moment $2.0 \, \mu_{\rm B}/{\rm Ni}^{2+}$, which leads to a g-factor as 2. Therefore, this saturation field suggests a J $\sim 5.9(6) \, \rm K$. The temperature dependence of the DC magnetic susceptibility $\chi(T)$ of single-crystal Ca₃NiNb₂O₉ sample is shown in Fig. 5. The data shows a peak around 4.2 K, indicating a magnetic ordering transition.

Figure 6 shows the temperature dependence of the AC susceptibility ($\chi'(T)$) of Ca₃CoNb₂O₉ measured with H//a (a) and H//c* (b). At zero field, two anomalies appear at $T_{\rm N1}=1.2$ K and $T_{\rm N2}=1.5$ K. The peak positions are independent of the frequency of the ac field (not shown here), indicating a two-step magnetic ordering. For H//a, both $T_{\rm N1}$ and $T_{\rm N2}$ decrease with increasing field. The $T_{\rm N1}$ feature disappears with field above 1.5 T. For H//c*, $T_{\rm N1}$ and $T_{\rm N2}$ decrease with increasing field too. The features of $T_{\rm N1}$ and $T_{\rm N2}$ don't show obvious differences between them.

Measurements on magnetic field dependence of AC susceptibility $(\chi'(H))$ were also carried out for $Ca_3CoNb_2O_9.$ The scans with $H//c^*$ didn't show any clear features and were not shown here. The scans with H//a were plotted in Fig. 6c. To clarify possible phase transitions, we used the 2.5 K data as a background and subtracted it from other low temperature data. Therefore, the data shown in Fig. 6c is $\Delta\chi'=\chi'(H,\,T)\!\!-\!\!\chi'(H,\,2.5\,K).$ The data at 0.02 K shows two clear anomalies at $H_{a1}=1.4\,T$ and $H_{a2}=3.3\,T$ below saturation field $H_S=5.8\,T.$ These features agree well with what we observed from the dc magnetization data and again suggest the existence of UUD phase. The similarity between dM/dH and the $\chi'(H)$ data is expected from the nature of $\chi'(H)$ (directly probing the derivative of the DC magnetization). Both H_{a1} and H_{a2} decrease with increasing temperatures.

Specific heat.—Figures 7a and 7b show the temperature dependence of specific heat of $Ca_3CoNb_2O_9$ ($C_P(T)$) with H//a and H//c*, respectively. At zero field, two sharp peaks show at $T_{N1}=1.2$ K and $T_{N2}=1.5$ K, again supporting a two-step magnetic ordering. With increasing field along the a-axis and c*-axis, both T_{N1} and T_{N2} decrease and only T_{N2} is visible above 2 T. We note here that Dai et al. suggested a long-range anti-ferromagnetic order at 1.45 K followed by a spin glass ground state below 1.2 K from their works based on polycrystalline samples. The Considering the sharp T_{N2} 0 anomalies at both T_{N3} 1 from our data and the frequency-independent peaks in ac susceptibility, it is more likely that both transitions are with long-range ordering nature. Figure 7c shows the specific heat of T_{N3} 1 considering the sharp ordering transition with T_{N1} 1 and T_{N2} 2 decrease and T_{N2} 3 and T_{N2} 4.

Dielectric constant.—Figures 8a and 8b show the temperature dependence of the real part of the dielectric constant $\varepsilon'(T)$ of Ca₃CoNb₂O₉ with both H and electric field (E) applied along the

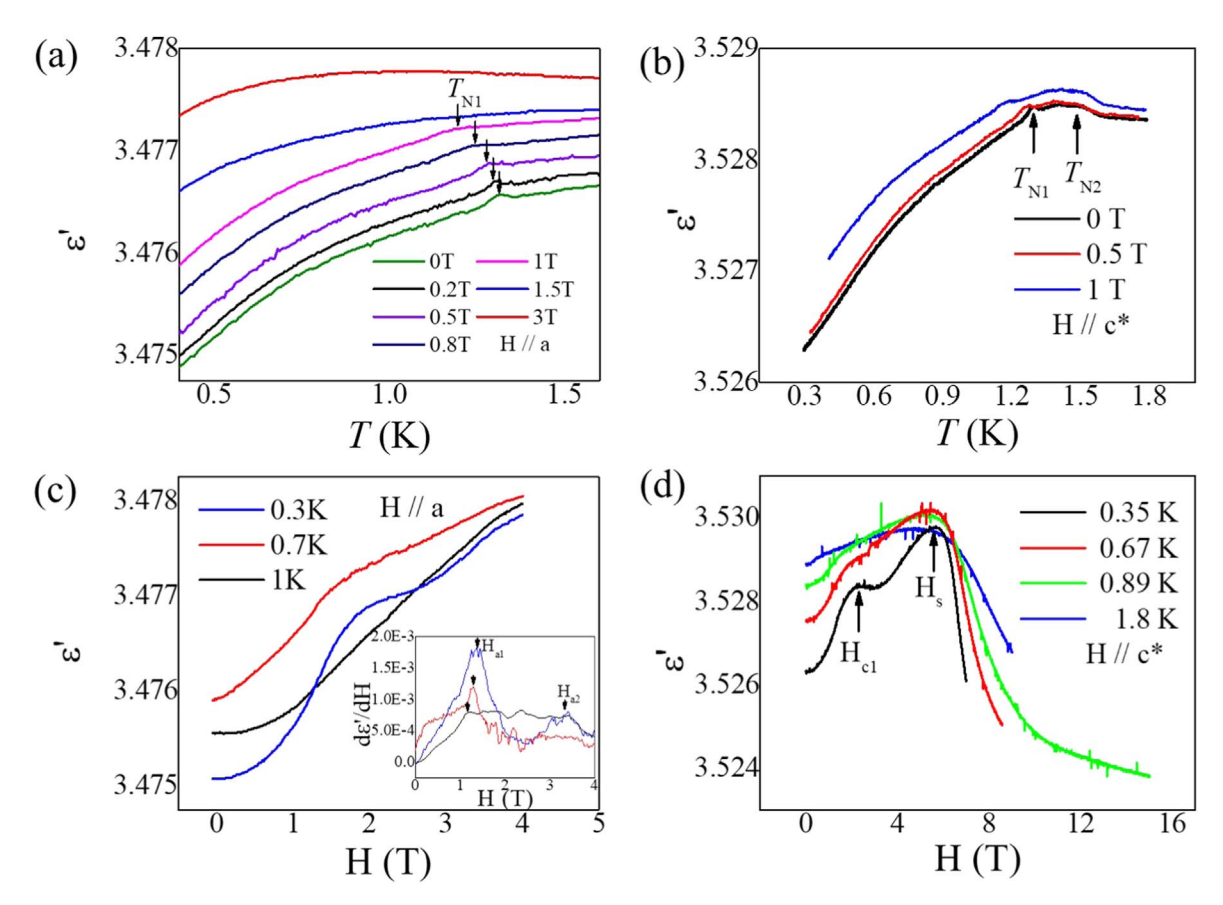


Figure 8. Temperature dependence of $\varepsilon'(T)$ of Ca₃CoNb₂O₉ at different fields with H//a (a) and H//c* (b). Data was offset by 0.003. The field dependence of $\varepsilon'(H)$ at different temperatures with H//a (c) and H//c*(d). Inset of (c): the derivative of the ε' with respect field.

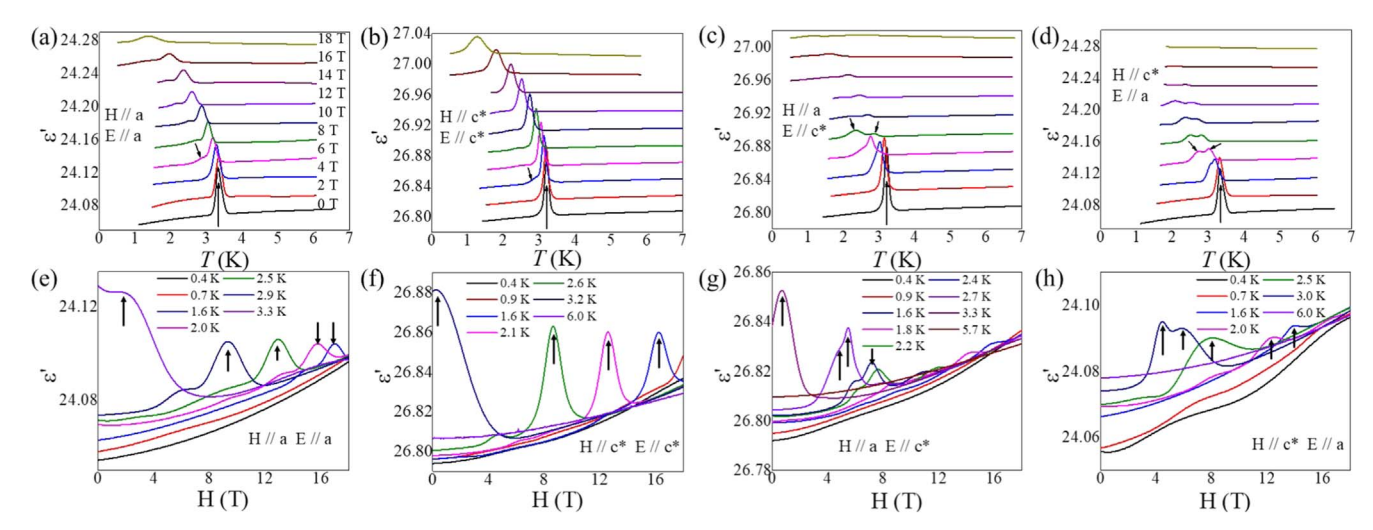


Figure 9. (a)–(d) Temperature dependence of $\varepsilon'(T)$ of Ca₃NiNb₂O₉ with H and E applied along the different crystallographic directions. Data was offset by 0.003. (e)–(h) Field dependence of the $\varepsilon'(H)$ of Ca₃NiNb₂O₉ with H and E applied along the different directions. The arrows represent the temperature or field positions at which the anomalies were observed on the $\varepsilon'(T)$ and $\varepsilon'(H)$ curves. These critical temperatures and fields were used to constructed the phase diagrams in Fig. 12.

a-axis or c*-axis, respectively. With H//a, a small peak appears at a temperature close to $T_{\rm N1}$ and there is no noticeable feature around $T_{\rm N2}$. With increasing fields, the $T_{\rm N1}$ peak shifts to lower temperatures and becomes weaker. It disappears eventually above 1 T. With H//c*, the $\varepsilon'(T)$ curve shows two anomalies at $T_{\rm N1}=1.3$ K and $T_{\rm N2}=1.5$ K. And both $T_{\rm N1}$ and $T_{\rm N2}$ decrease with increasing fields. As shown in Fig. 8c, with H//a, the field dependence of $\varepsilon'(H)$ measured at 0.3 K and 0.7 K show a broad peak between 1 T and 3 T. The derivative of $\varepsilon'(H)$ shows two anomalies more clearly at

 $1.3\,\mathrm{T}$ and $3.4\,\mathrm{T}$, which are again consistent with $\mathrm{H_{a1}}$ and $\mathrm{H_{a2}}$ observed from the ac susceptibility and dc magnetization. The peak becomes weaker as the temperature increases. The $\varepsilon'(\mathrm{H})$ curve with $\mathrm{H//c^*}$ also shows two anomalies. Here we assign them as $\mathrm{H_{c1}}$ and the saturation field $\mathrm{H_{s}}$, respectively. To investigate whether the anomalies in the dielectric constant origin from the ferroelectricity, we measured pyroelectric current while sweeping the temperature across the transitions. No noticeable pyroelectric current signals were observed (not shown here), hence no spontaneous electric

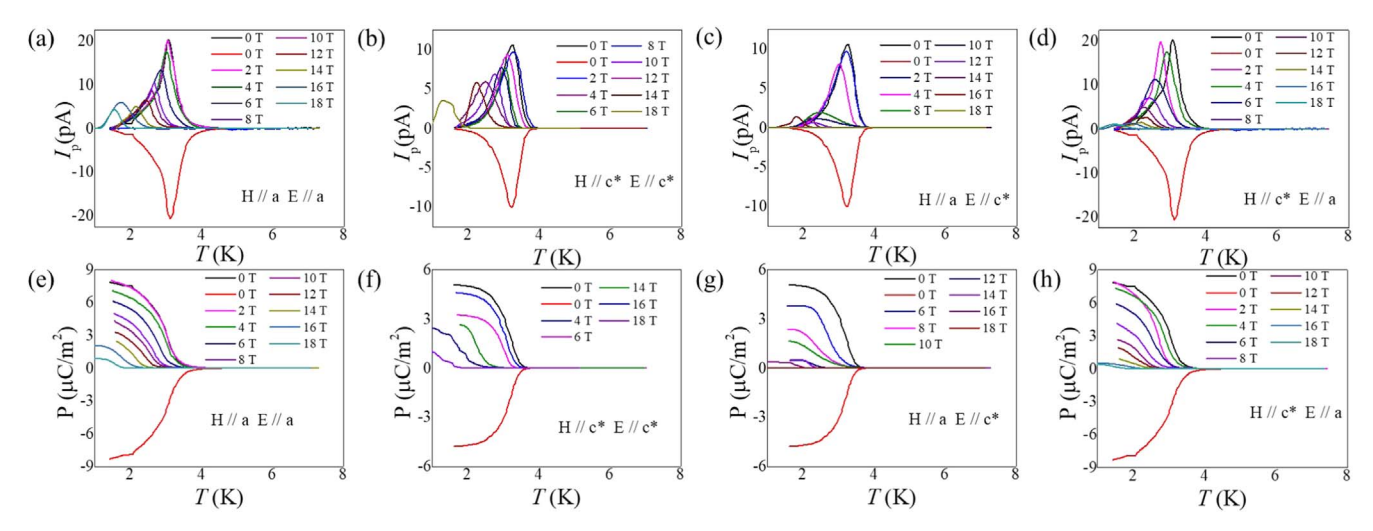


Figure 10. (a)—(d) Temperature dependence of the pyroelectric current of $Ca_3NiNb_2O_9$ with H and E applied along the different crystallographic directions. (e)—(h) Temperature dependence of polarization of $Ca_3NiNb_2O_9$ with H and E applied along different directions.

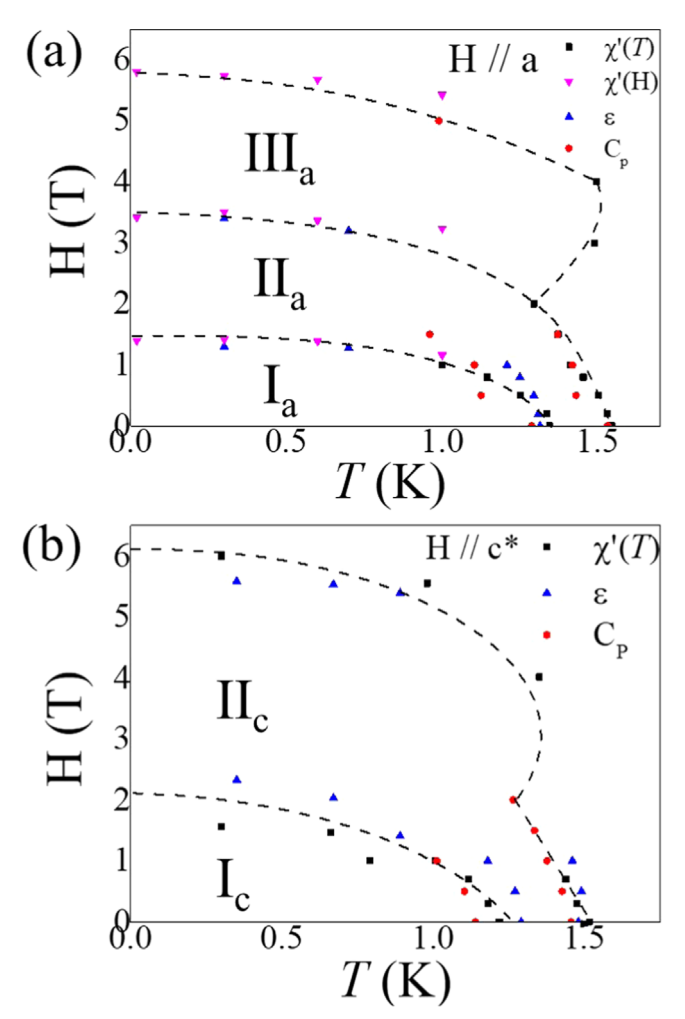


Figure 11. The magnetic phase diagrams of $Ca_3CoNb_2O_9$ with H//a (a) and H//c* (b).

polarization in $Ca_3CoNb_2O_9$. This is different from $Ba_3CoNb_2O_9$, where the ferroelectricity with spontaneous electric polarization of an order of $0.3\mu C$ m⁻² exist at all magnetically ordered states. ¹⁷ The weak feature in the dielectric constant in Fig. 8 already indicates a lack of a ferroelectric order, which would give a stronger dielectric

constant anomaly.³⁹ The absence of ferroelectricity in Ca₃CoNb₂O₉ and appearance of ferroelectricity in Ba₃CoNb₂O₉ could be related to their different magnetic ground states, which are stripe order in Ca₃CoNb₂O₉ but 120 degree ordering in Ba₃CoNb₂O₉.

In contrast to Ca₃CoNb₂O₉, Ca₃NiNb₂O₉ shows pronounced features in the dielectric constant measurements. Figures 9a-9d show the $\varepsilon'(T)$ measured with different combinations of H and E directions as H//a and E//a for (a), H//c* and E//c* for (b), H//a and E//c* for (c), H//c* and E//a for (d). Under zero field, there is only one strong anomaly in each curve at a temperature between T_{N1} and $T_{\rm N2}$. With H//a, the anomaly shifts to lower temperature with increasing field and remains obvious up to 18 T. Another weak anomaly shows up at lower temperature above 6 T with E//a and 4 T E//c*. With H//c*, the anomaly also shifts to lower temperature with increasing field, but the intensity decreases much quicker. Similarly, another low-temperature anomaly shows up above 4 T with both E//a and E//c*. Figures 9e-9h show the field dependence of the dielectric constant $\varepsilon'(H)$ with H and E applied in different directions. In all conditions, $\varepsilon'(H)$ shows several peak-and-valley features. The strongest peak shifts to higher fields and becomes weaker with decreasing temperature. These features observed from $\varepsilon'(T)$ and $\varepsilon'(H)$ are used to construct the phase diagrams of Ca₃NiNb₂O₉ in Fig. 12.

Polarization measurements were also performed on Ca₃NiNb₂O₉ to confirm the existence of ferroelectricity. Figures 10a-10d show the pyroelectric current measurements with different combinations of H and E directions. Figures 10e-10h show the corresponding spontaneous polarization (P), which was obtained by integrating the pyroelectric current with respect to time. In Figs. 10a-10d, a sharp peak of the pyroelectric current was observed below 4 K for all conditions. It shifts to low temperature and becomes weaker with increasing field. We observed that the polarization along a-axis is more significant than the polarization along c*-axis. Correspondingly, the polarization with E//a is more significant. Furthermore, the reversible polarization confirms the ferroelectric ground state in $Ca_3NiNb_2O_9$. The magnitude of the polarization at zero field is around 7.8 μC m⁻² with E//a, and 5.1 μ C m⁻² with E//c* for Ca₃NiNb₂O₉. These values are larger than the magnitude of the polarization for Ba₃NiNb₂O₉ (\sim 1.1 μ C m⁻²). ¹⁸ This could be due to the fact that the polarization for Ba₃NiNb₂O₉ is obtained on polycrystalline samples.

Discussion

Based on all the data presented above, magnetic phase diagrams of $Ca_3CoNb_2O_9$ and $Ca_3NiNb_2O_9$ are constructed.— $Ca_3CoNb_2O_9$ The phase diagram with H//a (Fig. 11a) shows more features than the one with H//c* (Fig. 11b) for $Ca_3CoNb_2O_9$.

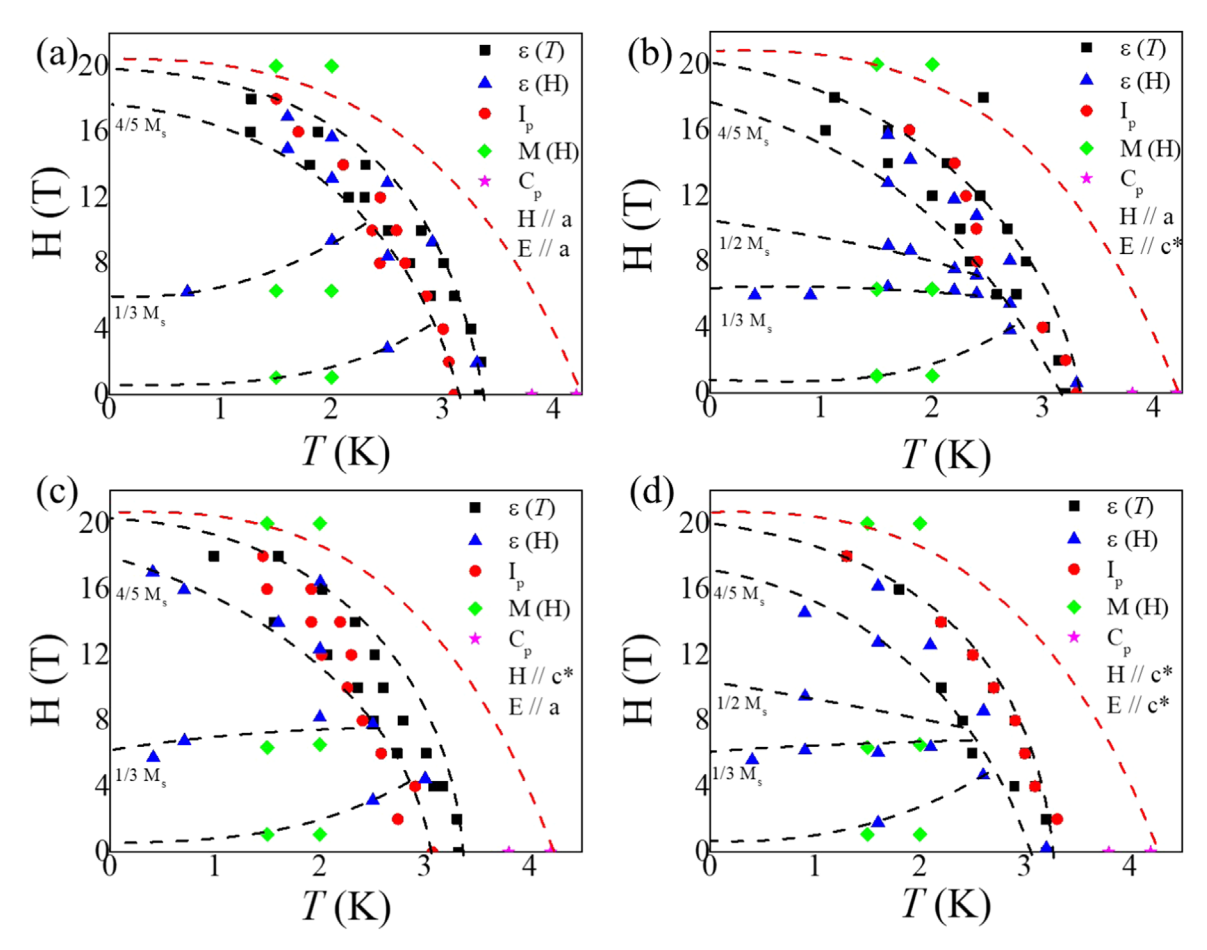


Figure 12. The magnetic phase diagrams of Ca₃NiNb₂O₉ with H//a, E//a (a), H//a, E//c* (b), H//c*, E//a (c), and H//c*, E//c* (d).

Therefore, we argue this compound has an easy-plane anisotropy. The theories have predicted successive magnetic phase transitions in TLAFs between Y, UUD with $1/3M_s$ and an oblique phase under the magnetic field. $^{40-42}$ In our work, three magnetic phases are identified in addition to the paramagnetic phase above T_{N2} and the polarized phase above H_s with H//a, which are quantitatively consistent with the theoretical studies. However, as we discussed in the previous section, the long-range ordered phase in this system at zero field is a stripe spin structure other than a 120 degree spin structure. The distortion in the triangular lattice induces spatial anisotropy and could be the reason for the appearance of a stripe ordered state. On the other hand, for $Ca_3NiNb_2O_9$, with similar lattice distortion, it still shows a 120 degree spin structure. Therefore, how the lattice distortion exactly affects the magnetic ground state could also depend on the spin number of $Ca_3MNb_2O_9$.

Since the zero-field ordered phase in $Ca_3CoNb_2O_9$ is different from the theories on the ideal triangular lattice. It is reasonable to argue that the low-field phase for H//a, I_a , is not the Y phase under the assumption. Here we name it as canted stripe phase. Phase II_a is assigned to be UUD because of the peak-valley-peak features around the 1/3 M_s in AC susceptibility measurements. The appearance of the UUD phase indicates that the Zeeman energy of spins in a higher magnetic field has dominated the Hamiltonian and the geometrical frustration persists under magnetic field so that the magnetic phase of our system starts to agree with the theories on the ideal triangular lattice. Following this consideration, we argue the phase III_a to be oblique phase since the magnetic field is even higher. Meanwhile, the UUD phase regime becomes larger with the decreasing temperature near T_N 's until its field range is almost unchanged below 1.0 K. This implies that the quantum fluctuations are influential in stabilizing the UUD phase. Chubukov I_a 0 estimated the critical fields

for such UUD phase in the case of isotropic Heisenberg TLAF using the spin-wave approach. Up to the first order of 1/S expansion, they obtained $H_{a1} = H_s/3(1 - 0.084/S)$ and $H_{a2} = H_s/3(1 + 0.215/S)$. In our case, with $H_s = 5.7 \text{ T}$ and S = 1/2, it gives $H_{a1} = 1.58 \text{ T}$, and $H_{a2} = 2.72 \text{ T}$. Experimentally, H_{a1} from our measurements agrees excellently with the calculation, while Ha2 is larger than the calculated one by 23%. This discrepancy may be due to the model being based on the equilateral TLAFs. The overall features of the UUD phase are similar to those of the low spin TLAFs such as Ba₃CoNb₂O₉ (Co²⁺, S = 1/2)¹⁷ and Ba₃NiNb₂O₉ (Ni²⁺, S = 1)¹⁸ but different from the large spin TLAFs such as Ba₃MnNb₂O₉ (Mn²⁺,S = 5/2),⁴³ RbFe(MoO₄)₂ (Fe³⁺, S = 5/2),^{44,45} where the UUD phase become less stable at low temperatures as the thermal fluctuations decrease. The fact that these two distinct groups can be classified solely by the magnitude of the spin is important evidence of the role of quantum fluctuations for the UUD phase. In Fig. 11b, the magnetic phase diagram with H//c* only shows two phases before fully polarized. More work is required to reveal the detailed spin configurations of these two phases. Here we tentatively assigned phase II_c as an oblique phase.

Another notable feature is the two-step phase transition from the paramagnetic phase to the ordering states at low fields (H « $\rm H_s/3$) in both directions. It has been predicted that when the magnetic anisotropy energy is negative, a two-step phase transition can be observed. It also suggests that the transitions at $T_{\rm N2}$ and $T_{\rm N1}$ correspond to a phase transition into the UUD phase and another phase transition into the low-field co-planar phase, respectively. Experimentally, a few compounds with easy-axis anisotropy showed the two-step phase transition at low fields. On the other hand, a single-step phase transition appears in a system with easy-plane anisotropy at low field regime.

anisotropy in the ab plane related to the lattice distortion, on top of the easy plane anisotropy, could be the reason for the two-step ordering process.

 $Ca_3NiNb_2O_9$ As shown in Fig. 12, the magnetic phase diagrams of Ca₃NiNb₂O₉ are more complicated because of the coexistence of ferroelectric ordering and magnetic ordering. Four phase diagrams are constructed with the different combinations of H and E directions. Here the red dashed lines are used to represent the rough boundary of the magnetic ordering phase based on the magnetization and specific heat measurements. The two-step phase transition should also origin from the spatial anisotropy, like in Ca₃CoNb₂O₉. Meanwhile, all the phase boundaries determined by dielectric constant and polarization measurements are inside the magnetic ordering phase. In all situations, a phase transition close to zero field can be observed, which represents a spin-flip transition according to magnetization measurements. With E//a (Figs. 12a and 12c), another two phase transitions appear around the fields with 1/3M_s and 4/5M_s. With E//c* (Figs. 12b and 12d), three more phase transitions appear around fields with 1/3M_s, 1/2M_s and 4/5M_s, respectively. The 1/3M_s phase transition can also be argued to be a spin-flip transition based on the magnetization curves, but this transition doesn't lead to an UUD phase with magnetization plateau according to the magnetization measurements. Furthermore, the origin of 1/2M_s and 4/5M_s phase transitions can't be fully understood by our current data, which needs further studies. A noteworthy part is that the number of phase transitions is related to the direction of the electric field other than the magnetic field.

Conclusions

In conclusion, our experiments on single crystalline Ca₃MNb₂O₀ show that they are TLAFs with spatial anisotropy. This spatial anisotropy is likely to lead to a two-step magnetic ordering with weak easy-plane anisotropy for both the Co and Ni samples. For Ca₃CoNb₂O₉, we observed a series of magnetic phase transitions with H//a and H//c*, starting from the stripe long-range ordering spin structure under zero field. This spin structure is different from the 120 degree spin structure and also eliminates the ferroelectricity in this compound. Meanwhile, the dielectric constant and pyroelectric current measurements for Ca₃NiNb₂O₉ with 120 degree spin structure as ground state clearly shows coexistence of ferroelectricity and spin state transitions, which is similar to that of Ba₃CoNb₂O₉ and Ba₃NiNb₂O₉. 18 It confirms that the ferroelectricity in such TLAFs is related to the 120 degree magnetic ordering structure.

Acknowledgments

Q. H. and H.D.Z. thank the support from NSF-DMR through Award DMR-2003117. J.M. thanks the financial support from the National Science Foundation of China (Nos. 11774223, and U2032213). This research used resources at the High Flux Isotope Reactor, a DOE Office of Science User Facility operated by the Oak Ridge National Laboratory. A portion of this work was performed at the NHMFL, which is supported by National Science Foundation Cooperative Agreement No. DMR-1157490 and the State of Florida. E. S. Choi and M. Lee acknowledge the support from NSF-DMR-1309146.

ORCID

M. Lee https://orcid.org/0000-0002-2369-9913 H. D. Zhou https://orcid.org/0000-0002-1595-1912

References

- 1. P. W. Anderson, Mater. Res. Bull., 8, 153 (1973).
- 2. L. Balents, Nature, 464, 199 (2010).
- 3. X. G. Wen, Int. J. Mod. Phys. B, 4, 239 (1990).
- 4. G. Wannier, Phys. Rev., 79, 357 (1950).
- 5. P. W. Anderson, G. Baskaran, Z. Zou, and T. Hsu, Phys. Rev. Lett., 58, 2790 (1987)
- 6. D. A. Huse and V. Elser, *Phys. Rev. Lett.*, **60**, 2531 (1988).
- B. Bernu, C. Lhuillier, and L. Pierre, *Phys. Rev. Lett.*, **69**, 2590 (1992).
 N. Elstner, R. Singh, and A. Young, *Phys. Rev. Lett.*, **71**, 1629 (1993).
- L. Capriotti, A. E. Trumper, and S. Sorella, *Phys. Rev. Lett.*, **82**, 3899 (1999).
 H. Kawamura, *J. Phys. Soc. Jpn.*, **53**, 2452 (1984).
- 11. H. Kawamura and S. Miyashita, J. Phys. Soc. Jpn., 54, 4530 (1985).
- 12. A. V. Chubukov, *Physical Review B*, 44, 4693 (1991).
- 13. J. Ma, Y. Kamiya, T. Hong, H. Cao, G. Ehlers, W. Tian, C. Batista, Z. Dun, H. Zhou, and M. Matsuda, *Phys. Rev. Lett.*, 116, 087201 (2016).
- 14. S. Korshunov, J. Phys. C: Solid State Phys., 19, 5927 (1986).
- 15. T. Susuki, N. Kurita, T. Tanaka, H. Nojiri, A. Matsuo, K. Kindo, and H. Tanaka, Phys. Rev. Lett., 110, 267201 (2013).
- 16. N. A. Fortune, Q. Huang, T. Hong, J. Ma, E. Choi, S. T. Hannahs, Z. Zhao, X. Sun, Y. Takano, and H. Zhou, *Physical Review B*, **103**, 184425 (2021).
- 17. M. Lee, J. Hwang, E. Choi, J. Ma, C. D. Cruz, M. Zhu, X. Ke, Z. Dun, and H. Zhou, Physical Review B, 89, 104420 (2014).
- 18. J. Hwang, E. Choi, F. Ye, C. D. Cruz, Y. Xin, H. Zhou, and P. Schlottmann, Phys. Rev. Lett., 109, 257205 (2012).
- 19. Y. Shirata, H. Tanaka, T. Ono, A. Matsuo, K. Kindo, and H. Nakano, J. Phys. Soc. Jpn., 80, 093702 (2011).
- 20. K. Ranjith, K. Brinda, U. Arjun, N. Hegde, and R. Nath, J. Phys. Condens. Matter, 29, 115804 (2017).
- 21. B. Xu, W. Zhang, X.-Y. Liu, J. Ye, W. Zhang, L. Shi, X. Wan, J. Yin, and Z. Liu, Physical Review B, 76, 125109 (2007).
- 22. Z. Lu, L. Ge, G. Wang, M. Russina, G. G. ünther, C. dela Cruz, R. Sinclair, H. Zhou, and J. Ma, *Physical Review B*, 98, 094412 (2018).
- 23. M. Lee, E. S. Choi, J. Ma, R. Sinclair, C. R. DelaCruz, and H. D. Zhou, Mater. Res. Bull., 88, 308 (2017).
- 24. T. Kimura, T. Goto, H. Shintani, K. Ishizaka, T.-h Arima, and Y. Tokura, Nature, **426**, 55 (2003).
- N. A. Spaldin and M. Fiebig, *Science*, **309**, 391 (2005).
 M. Fiebig, *J. Phys. D: Appl. Phys.*, **38**, R123 (2005).
- 27. Y. Tokura, *Science*, **312**, 1481 (2006).
- 28. S.-W. Cheong and M. Mostovoy, Nat. Mater., 6, 13 (2007).
- 29. K. Wang, J.-M. Liu, and Z. Ren, Adv. Phys., 58, 321 (2009).
- 30. H. Katsura, N. Nagaosa, and A. V. Balatsky, *Phys. Rev. Lett.*, **95**, 057205 (2005).
- 31. T.-h Arima, J. Phys. Soc. Jpn., 76, 073702 (2007).
- 32. C. Jia, S. Onoda, N. Nagaosa, and J. H. Han, *Physical Review B*, 76, 144424 (2007).
- 33. M. Mostovoy, Phys. Rev. Lett., 96, 067601 (2006).
- 34. A. J. Hearmon, F. Fabrizi, L. C. Chapon, R. Johnson, D. Prab-hakaran, S. V. Streltsov, P. Brown, and P. G. Radaelli, *Phys. Rev. Lett.*, 108, 237201 (2012).
- 35. H. Mitamura et al., Phys. Rev. Lett., 113, 147202 (2014).
- 36. J. Rodr´ıguez-Carvajal, *Physica B*, **192**, 55 (1993).
- 37. J. Dai, P. Zhou, P.-S. Wang, F. Pang, T. J. Munsie, G. M. Luke, J.-S. Zhang, and W. Yu, Chinese Phys. B, 24, 127508 (2015).
- 38. V. Ting, Y. Liu, L. Noren, R. Withers, D. Goossens, M. James, and C. Ferraris, . Solid State Chem., 177, 4428 (2004).
- 39. S. Seki, Y. Onose, and Y. Tokura, Phys. Rev. Lett., 101, 067204 (2008).
- 40. G. Koutroulakis, T. Zhou, Y. Kamiya, J. Thompson, H. Zhou, C. Batista, and S. Brown, *Physical Review B*, **91**, 024410 (2015).
- 41. L. Seabra, T. Momoi, P. Sindzingre, and N. Shannon, Physical Review B, 84, 214418 (2011).
- 42. D. Yamamoto, G. Marmorini, and I. Danshita, Phys. Rev. Lett., 112, 127203 (2014).
- 43. M. Lee, E. Choi, X. Huang, J. Ma, C. D. Cruz, M. Matsuda, W. Tian, Z. Dun, S. Dong, and H. Zhou, *Physical Review B*, 90, 224402 (2014).
- 44. A. Smirnov, H. Yashiro, S. Kimura, M. Hagiwara, Y. Narumi, K. Kindo, A. Kikkawa, K. Katsumata, A. Y. Shapiro, and a L. Demianets, Physical Review B, 75, 134412 (2007).
- 45. L. Svistov, A. Smirnov, L. Prozorova, O. Petrenko, A. Micheler, N. B. uttgen, A. Y. Shapiro, and L. Demianets, Physical Review B, 74, 024412 (2006).
- 46. M. Collins and O. Petrenko, Can. J. Phys., 75, 605 (1997).
- 47. R. Clark and W. Moulton, Physical Review B, 5, 788 (1972)
- 48. S. Maegawa, T. Kohmoto, T. Goto, and N. Fujiwara, *Physical Review B*, 44, 12617 (1991).
- 49. H. Kadowaki, T. Inami, Y. Ajiro, K. Nakajima, and Y. Endoh, J. Phys. Soc. Jpn., 60, 1708 (1991).
- 50. B. Gaulin, T. Mason, M. Collins, and J. Larese, Phys. Rev. Lett., 62, 1380 (1989).